Available online at www.sciencedirect.com
ScienceDirect
International Journal of Heat and Mass Transfer 50 (2007) 4823–4832
International Journal of HEAT and MASS TRANSFER
www.elsevier.com/locate/ijhmt

On the behaviour of hygroscopic wheels: Part II – rotor performance

C.R. Ruivo [a,b,*], J.J. Costa [b], A.R. Figueiredo [b]

[a] Área Departamental de Engenharia Mecânica, Escola Superior de Tecnologia, Universidade do Algarve, Campus da Penha, 8005-139 Faro, Portugal
[b] ADAI, Department of Mehanical Engineering, University of Coimbra, P 3030-788 Coimbra, Portugal

Received 19 January 2006; received in revised form 25 February 2007
Available online 10 May 2007

Abstract

The simplified model developed in Part I for the behaviour of a channel with parallel desiccant walls is adapted and used to analyse heat and mass transfer phenomena in hygroscopic rotors, the so-called enthalpy wheels and desiccant wheels, operating in steady-state conditions. The characterization of the corrugated matrix and an inspection of the effect of the corrugate curvature are presented. Global parameters characterizing the performance of the hygroscopic rotor are defined, and evaluated after the numerical results for the cyclic stationary behaviour of a real shape channel. Parametric studies are presented, concerning the steady-state performance of an equally partitioned desiccant wheel having sinusoidal-type channels. The influences of the dimensions of the matrix cells and of the constitution and thickness of the channel walls, as well as of the rotation speed and the inlet airflow conditions on the performance of desiccant wheels were analysed. The results presented provide a powerful insight into the operation of this type of devices, the model being an interesting tool both for manufacturing and design purposes.

Keywords: Solid desiccant; Corrugated matrix; Hygroscopic rotor; Steady-state behaviour

1. Introduction

Hygroscopic rotors have been applied for decades as enthalpy wheels in energy recovery processes, as well as desiccant wheels in applications of air dehumidification.

Studies of the global behaviour of air conditioning systems integrating desiccant wheels have been performed exclusively on an experimental basis [1–5] or by way of numerical simulation techniques. In the latter cases, the necessary characterization of the behaviour of the desiccant wheel was obtained by laboratory experiments [6,7], either using directly the performance data provided by the manufacturer [8,9] or by using specific software [10–14].

Other studies have been dedicated to the behaviour of hygroscopic rotors. Concerning the desiccant wheels, experiments have been done to validate prediction physical models [15–22], simplified models have been developed using experimental data correlations [23–25] and the performance characterization has been performed by carrying out experiments under various operating conditions [26–29]. Another series of works was dedicated to the experimental investigation of the behaviour of enthalpy wheels [30–34]. In other studies, based on advanced physical models, the internal sorption and diffusion transport was taken as local phenomena in the thin desiccant layer of the matrix [35–40].

The simplified model described in Part I of this paper is adapted to simulate the cyclic behaviour of the channel of a corrugate matrix, and then used to predict the heat and mass transfer in a hygroscopic rotor operating at steady-state conditions.

2. Geometric parameters and convection transfer in the matrix

In Fig. 1, three matrix cells with distinct corrugations are schematically represented, illustrating its typical

* Corresponding author. Address: Área Departamental de Engenharia Mecânica, Escola Superior de Tecnologia, Universidade do Algarve, Campus da Penha, 8005-139 Faro, Portugal. Tel.: +351 289 800100; fax: +351 289 888405.
E-mail address: cruivo@ualg.pt (C.R. Ruivo).

0017-9310/$ - see front matter © 2007 Elsevier Ltd. All rights reserved.
doi:10.1016/j.ijheatmasstransfer.2007.03.004

Nomenclature

a_s	specific transfer area of the matrix
$\bar{c}^*_{p_{f,out}}$	specific heat of the bulk airflow referred to the unit of mass of the mixture
d_{hyd}	hydraulic diameter
$d\theta$	infinitesimal angle of the elementary volume of the wheel
$d\tau$	infinitesimal time step
E_p	plate thickness (Fig. 1)
$F_{m,in}$	inlet convective intensity (or mass velocity)
H_c	half-height of the modelled channel
H_d	thickness of the desiccant layer
H_p	half-thickness of the modelled channel wall ($H_p = H_d + H_{sub} = 0.5E_p$)
H_{sin}	characteristic dimension of the sinusoidal-type corrugated matrix (cf. Fig. 2)
H_{sub}	half-thickness of the substrate layer of the modelled channel
$\dot{J}_{v,gs}$	mass transfer rate per unit of transfer area of the modelled channel
$\dot{J}^{\#}_m$	mass transfer rate per unit of frontal area of the matrix
L_c	channel length
Nu	Nusselt number
P_{cell}	cell pitch (Fig. 1)
P_{sin}	characteristic dimension of the sinusoidal-type corrugated matrix (cf. Fig. 2)
$P_{w,cell}$	wetted perimeter of the cell
$\dot{Q}_{h,gs}$	heat transfer rate per unit of transfer area of the modelled channel
$\dot{Q}^{\#}_h$	heat transfer rate per unit of frontal area of the matrix
R	radius of the hygroscopic wheel (Fig. 5)
r	spatial coordinate (Figs. 2 and 5)
S_p	length of contact area (cf. Fig. 1)
T	temperature
t	time coordinate
w_v	water-vapour content in the gas mixture
$X_{\ell,i}$	adsorbed water content in the porous medium at the interface (d.b.)
x, y	spatial coordinates

Greek symbols

α_{sin}	characteristic aspect ratio of the cell P_{sin}/H_{sin}
δ_{sin}	characteristic dimension of the sinusoidal-type corrugated matrix (cf. Fig. 2)
ε_m	porosity of the matrix
φ_v	vapour mass fraction of the gas mixture
θ	angular coordinate in the hygroscopic rotor (Fig. 5)
ρ_f	density of bulk airflow
τ	time coordinate in an adsorption/desorption cycle
τ^+	dimensionless time coordinate in a adsorption/desorption cycle

Subscripts

ads	relative to the adsorption mode
cyc	relative to the adsorption/desorption cycle
des	relative to the desorption mode
f	bulk airflow
h	heat
i	solid-airflow interface
in	inlet condition
m	mass
out	outlet condition

dimensions, namely, the pitch P_{cell}, the height H_{cell}, the thickness of the plates E_p and the length S_p of the contact area between plane and wavy plates. It should be mentioned that the sinusoidal type corrugation provides higher specific transfer area, provided S_p is small.

In some real matrices, the cell exhibits a curvature as shown in Fig. 2, corresponding to two adjacent channels with opposite curvatures, as illustrated in Fig. 3, the cross section area being larger for the channel represented in Fig. 3a. The curved cell of the sinusoidal type corrugation is characterised by the aspect ratios P_{sin}/H_{sin} and δ_{sin}/P_{sin}.

The curvature aspect ratio δ_{sin}/P_{sin} depends on the radial position of the cell in the matrix, increasing in the direction of the rotor axis. The graphical representation of Fig. 4 characterizes this dependence relatively to the parameter P_{sin}/r, allowing to conclude that the curvature of the corrugation becomes negligible for $r > 2.5P_{sin}$, if the criterion $\delta_{sin}/P_{sin} < 0.05$ is adopted. Taking into account the dimensions of real rotors and of the corrugations, the curvature effect appears to be insignificant, even in less compact matrices, affecting only a very small fraction of the frontal area around the axis of the rotor.

For each corrugation represented in Fig. 1, it is possible to relate the wetted perimeter, the specific transfer area and the porosity with the pitch, the height and the wall thickness of the cell. Taking into account the expression proposed by [42], the cell wetted perimeter for sinusoidal type corrugation can be estimated as:

$$P_{w,cell} = 2H_{sin}\left[\alpha_{sin} + \sqrt{\alpha_{sin}^2 + \pi^2}\,\frac{3 + (2\alpha_{sin}/\pi)^2}{4 + (2\alpha_{sin}/\pi)^2}\right] - 4S_p, \quad (1)$$

where $\alpha_{sin} = P_{sin}/H_{sin}$.

The specific transfer area of each cell is evaluated as:

$$a_s = 2\frac{H_{sin}}{P_{cell}H_{cell}}\left[\alpha_{sin} + \sqrt{\alpha_{sin}^2 + \pi^2}\,\frac{3 + (2\alpha_{sin}/\pi)^2}{4 + (2\alpha_{sin}/\pi)^2}\right] - \frac{4S_p}{P_{cell}H_{cell}} \quad (2)$$

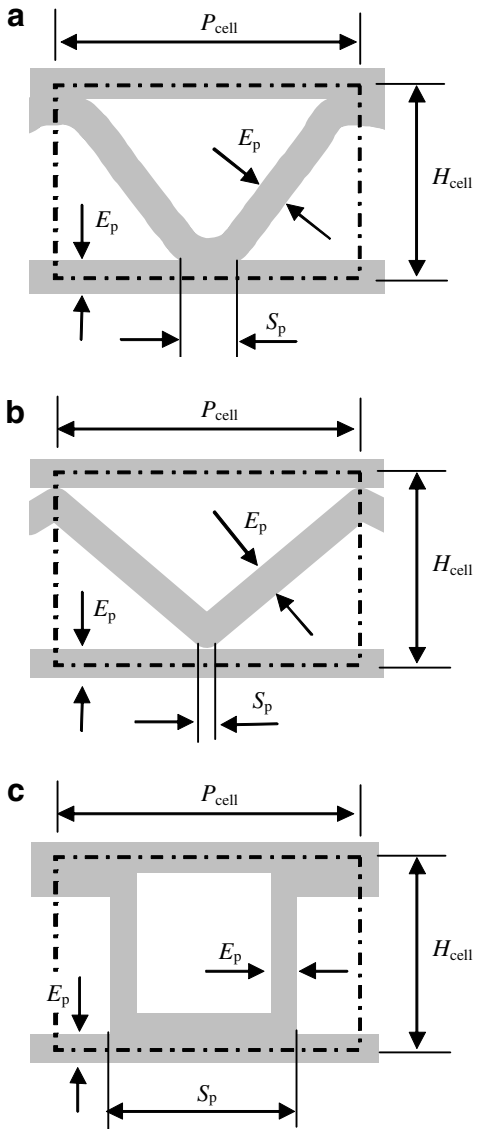

Fig. 1. Characteristic dimensions of the corrugation of (a) sinusoidal, (b) triangular and (c) rectangular type cells.

and the porosity of each cell is approximately determined by:

$$\varepsilon_m = 1 - \frac{E_p H_{sin}}{P_{cell} H_{cell}} \left[\alpha_{sin} + \sqrt{\alpha_{sin}^2 + \pi^2} \frac{3 + (2\alpha_{sin}/\pi)^2}{4 + (2\alpha_{sin}/\pi)^2} \right]. \quad (3)$$

With the porosity and the specific transfer area, the hydraulic diameter yields $d_{hyd} = 4\varepsilon_m/a_s$. When E_p is very small relatively to the dimensions of the cell, it can be assumed that $P_{cell} = P_{sin}$ and $H_{cell} = H_{sin}$, yielding to $\alpha_{sin} = P_{cell}/H_{cell}$. When E_p is significant and $S_P \approx 0$, the assumption $P_{cell} = P_{sin}$ remains valid, but a correction for H_{cell} must be adopted. The relation proposed is:

$$H_{cell} = H_{sin} + E_p + E_p \sqrt{1 + 4\alpha_{sin}^{-2}}. \quad (4)$$

In the literature, one can find Nusselt number values for several channel configurations, for completely developed

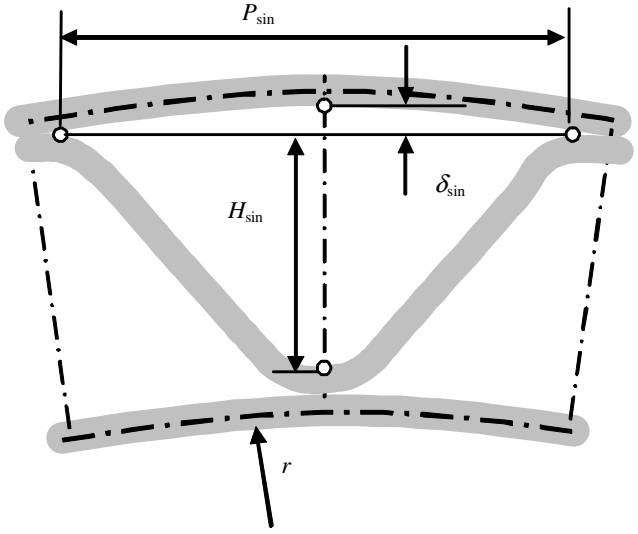

Fig. 2. Curved cell of a real matrix.

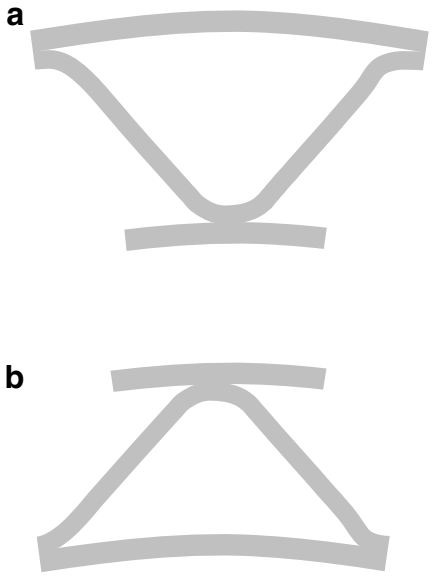

Fig. 3. Adjacent channels with (a) greater and (b) smaller cross section area.

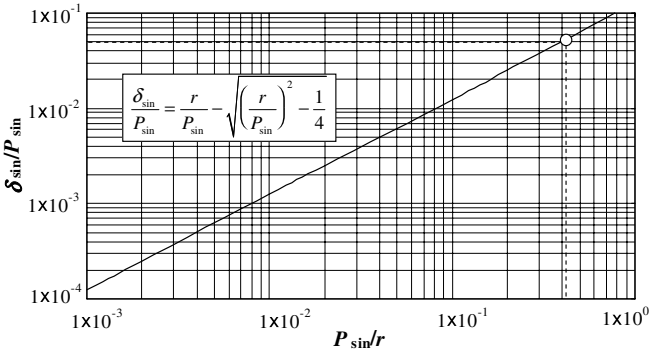

Fig. 4. Curvature of the matrix corrugation [41].

Table 1
Nusselt numbers for channels of sinusoidal corrugation type [45]. (Nu_A and Nu_B refer to the channel configurations of Fig. 3a and b, respectively.)

δ_{sin}/P_{sin}	H_{sin}/P_{sin}	Nu_A	Nu_B	$\overline{N}u_{AB}$
0	0.75	2.32	2.32	2.32
0.125	0.75	2.78	1.67	2.22
0.25	0.75	3.08	0.97	2.03
0	1.0	2.46	2.46	2.46
0.125	1.0	2.83	1.97	2.40
0.25	1.0	3.00	1.35	2.18
0	2.0	2.66	2.66	2.66
0.125	2.0	2.79	2.39	2.59
0.25	2.0	2.82	1.99	2.41

laminar flow with constant properties of the fluid [43,44]. For channels of sinusoidal corrugation type, Niu and Zhang [45] have numerically determined Nu values for the uniform and constant interface temperature condition and evaluating its dependence on the ratio δ_{sin}/P_{sin}. Some of the results of that work are compiled in Table 1, namely Nu_A and Nu_B for the channel types represented in Fig. 3a and b, respectively, showing that $Nu_A > Nu_B$. Moreover, it is seen that the deviations from the average value, $\overline{N}u_{AB} = 0.5(Nu_A + Nu_B)$, are directly proportional to the corrugation curvature, becoming important only in cases where $\delta_{sin}/P_{sin} > 0.125$. This conclusion, together with the fact that in real matrix of hygroscopic wheels δ_{sin}/P_{sin} is typically less lower than 0.05, means that a Nusselt number value given for a channel with no curvature effect ($\delta_{sin} = 0$) is precise enough for numerical modelling purposes. According to the results of Niu and Zhang [45], the following expression is proposed:

$$Nu = -0.2711\left(\frac{H_{sin}}{P_{sin}}\right)^2 + 1.018\frac{H_{sin}}{P_{sin}} + 1.7045. \quad (5)$$

3. Model for the stationary behaviour of a hygroscopic rotor

The detailed modelling of the behaviour of a hygroscopic rotor generally involves several difficulties, such as the complex channel geometry, the presence of structural elements in the rotor matrix, the non-uniform inlet conditions and the air crossover between the adsorption and desorption zones.

In Part I of this paper, a detailed two-dimensional numerical model (MD) was developed for the interaction between a moist airflow and the desiccant, plane parallel walls of a static channel. This model was taken as a reference to assess the quality of the results of a more simplified model (MS), which is based on the hypothesis of bulk airflow inside the channel, with the heat and mass fluxes at the interface modelled through appropriate convection coefficients. In view of the good agreement obtained, the simplified model MS is now adapted to simulate the transient cyclic behaviour of real shape channels of hygroscopic rotors. Since the channel wall thickness is one order of magnitude lower than its cross section dimensions, the two-dimensional formulation is kept, the real channel being approached by an equivalent parallel plate configuration with the same wall thickness and the real ratio of airflow rate to wetted perimeter. The convective heat and mass fluxes are calculated after the values of Nusselt and Sherwood numbers for the real channel geometry. It is assumed that the radial gradients in the matrix are negligible and that there are no significant transport phenomena between adjacent channels.

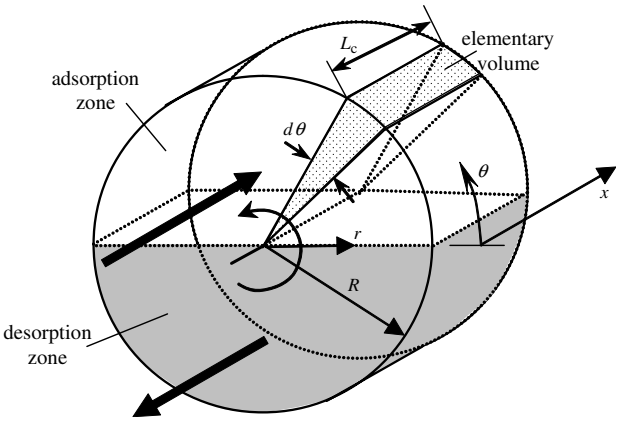

Fig. 5. Hygroscopic wheel.

The modelled channel is supposed to be representative of a rotating elementary volume of the wheel, such as the slice sketched in Fig. 5, which occupies successive angular positions θ. The simulation of the stationary behaviour of the wheel is achieved by cyclically changing the inlet airflow conditions and reversing the airflow direction in the channel, at the moment of transition between the adsorption and the desorption zones, thus reproducing the sequence of adsorption/desorption cycles.

In the modelled parallel plate geometry, the channel half-height and the half-thickness of the wall are $H_c = \varepsilon_m/a_s$ and $H_p = (1-\varepsilon_m)/a_s$, respectively, where ε_m and a_s are the porosity and the specific transfer area of the matrix. Additionally, to guaranty the real ratio of airflow rate to wetted perimeter in each zone of the matrix, the specification of each inlet condition must be based on a frontal velocity given by $u_{in} = F_{m,in}/\rho_{f,in}$, where $F_{m,in}$ represents the inlet airflow rate per unit of frontal area in each zone.

The cyclic process with a duration τ_{cyc} is divided into the adsorption and the desorption modes, with durations τ_{ads} and τ_{des}, respectively, the corresponding zones of the matrix being defined by $0 < \theta \leqslant \theta_{ads}$ and $\theta_{ads} < \theta \leqslant 2\pi$, with $\theta_{ads} = 2\pi\tau_{ads}/\tau_{cyc}$. From the point of view of the modelled channel, the adsorption and the desorption processes occur when $0 < \tau \leqslant \tau_{ads}$ and $\tau_{ads} < \tau \leqslant \tau_{cyc}$, respectively, with $\tau = \tau_{cyc}\theta/(2\pi)$.

For the stationary regime of the hygroscopic rotor, the transfer rates occurring in the adsorption zone are equal to those occurring in the desorption zone. Therefore, considering the adsorption mode, the following expressions can de deduced for the heat and mass transfer rates per unit of frontal area of the matrix, respectively:

$$\dot{J}_{\mathrm{m}}^{\#} = \frac{a_{\mathrm{s}} L_{\mathrm{c}}}{\tau_{\mathrm{cyc}}} \int_0^{\tau_{\mathrm{ads}}} \dot{J}_{\mathrm{v,gs}} \mathrm{d}\tau, \tag{6}$$

and

$$\dot{Q}_{\mathrm{h}}^{\#} = \frac{a_{\mathrm{s}} L_{\mathrm{c}}}{\tau_{\mathrm{cyc}}} \int_0^{\tau_{\mathrm{ads}}} \dot{Q}_{\mathrm{h,gs}} \mathrm{d}\tau, \tag{7}$$

parameters that have a practical interest for design purposes.

At the outlet of each zone, the air state exhibits a non-uniform angular distribution, and the downstream average temperatures are evaluated by:

$$T_{\mathrm{out,ads}} = \int_0^{\tau_{\mathrm{ads}}} \rho_{\mathrm{f,out}} \bar{c}^{*}_{\mathrm{p_{f,out}}} u_{\mathrm{out}} T_{\mathrm{out}} \mathrm{d}\tau \Big/ \int_0^{\tau_{\mathrm{ads}}} \rho_{\mathrm{f,out}} \bar{c}^{*}_{\mathrm{p_{f,out}}} u_{\mathrm{out}} \mathrm{d}\tau \tag{8}$$

and

$$T_{\mathrm{out,des}} = \int_{\tau_{\mathrm{ads}}}^{\tau_{\mathrm{cyc}}} \rho_{\mathrm{f,out}} \bar{c}^{*}_{\mathrm{p_{f,out}}} u_{\mathrm{out}} T_{\mathrm{out}} \mathrm{d}\tau \Big/ \int_{\tau_{\mathrm{ads}}}^{\tau_{\mathrm{cyc}}} \rho_{\mathrm{f,out}} \bar{c}^{*}_{\mathrm{p_{f,out}}} u_{\mathrm{out}} \mathrm{d}\tau, \tag{9}$$

respectively, for the outlet of the adsorption and desorption zones. The average outlet moisture contents are evaluated in a similar way by:

$$w_{\mathrm{v,out,ads}} = \int_0^{\tau_{\mathrm{ads}}} (1-\varphi_{\mathrm{v,out}}) \rho_{\mathrm{f,out}} u_{\mathrm{out}} w_{\mathrm{v,out}} \mathrm{d}\tau \Big/ \int_0^{\tau_{\mathrm{ads}}} (1-\varphi_{\mathrm{v,out}}) \rho_{\mathrm{f,out}} u_{\mathrm{out}} \mathrm{d}\tau \tag{10}$$

and

$$w_{\mathrm{v,out,des}} = \int_{\tau_{\mathrm{ads}}}^{\tau_{\mathrm{cyc}}} (1-\varphi_{\mathrm{v,out}}) \rho_{\mathrm{f,out}} u_{\mathrm{out}} w_{\mathrm{v,out}} \mathrm{d}\tau \Big/ \int_{\tau_{\mathrm{ads}}}^{\tau_{\mathrm{cyc}}} (1-\varphi_{\mathrm{v,out}}) \rho_{\mathrm{f,out}} u_{\mathrm{out}} \mathrm{d}\tau. \tag{11}$$

The variables $\rho_{\mathrm{f,out}}$, $\bar{c}^{*}_{\mathrm{p_{f,out}}}$, u_{out}, T_{out}, $\varphi_{\mathrm{v,out}}$ and $w_{\mathrm{v,out}}$ concern the outlet state of bulk airflow of the modelled channel as predicted by the present simplified model MS.

4. Parametric studies

Different parametric studies were conducted, in order to characterise the importance of a set of parameters on the behaviour of a hygroscopic wheel, namely the rotation speed, the cell dimensions, the wall thickness, as well as the inlet conditions of both airflows.

The shape of the matrix channel studied is illustrated in Fig. 6, and the different sizes of the cells are indicated in Table 2 (high, medium and low values of specific transfer area of the matrix, respectively, types A, B and C). The cells of each type have the same H_{cell} and P_{cell}, and different wall thickness E_{p}, leading to different values of H_{sin}, ε_{m} and a_{s}. It is assumed that $S_{\mathrm{p}} = 0$, meaning that the corrugation has its maximum specific transfer area (cf. Fig. 1).

The properties of the desiccant considered are those of silica gel RD, and can be found in Part I of this paper. The values of the specific heat, the density and the thermal conductivity of the substrate are supposed to be the same of the silica gel RD. Following the procedure described in Part I, the convective coefficients are evaluated after the Nusselt number estimated by Eq. (5).

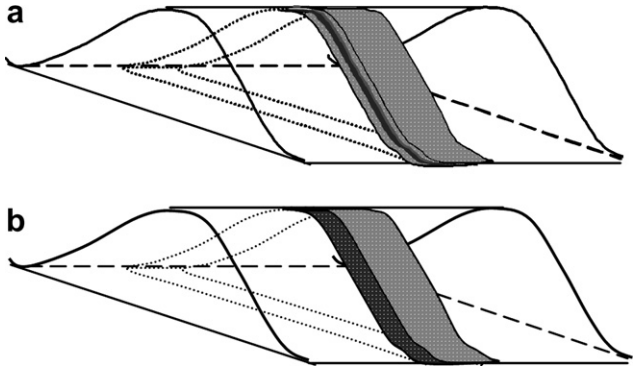

Fig. 6. Sketch of a sinusoidal channel with the wall composed by (a) separate layers of substrate and desiccant (wall type I) and (b) substrate and desiccant mixed in a single layer (wall type II).

Table 2
Characteristic geometric parameters of cells of type A, B and C ($P_{\mathrm{cell}} = P_{\mathrm{sin}}$)

		E_{p} (mm)	H_{sin} (mm)	ε_{m}	a_{s} ($\mathrm{m^2\,m^{-3}}$)
Cells type A:	A1	0.05	0.88	0.878	4852
$H_{\mathrm{cell}} = 1$ mm	A2	0.075	0.83	0.821	4769
$P_{\mathrm{cell}} = 2$ mm	A3	0.1	0.77	0.766	4673
	A4	0.25	0.47	0.467	4267
Cells type B:	B1	0.05	1.38	0.918	3280
$H_{\mathrm{cell}} = 1.5$ mm	B2	0.075	1.33	0.879	3239
$P_{\mathrm{cell}} = 3$ mm	B3	0.1	1.27	0.84	3198
	B4	0.25	0.95	0.627	2980
Cells type C:	C1	0.05	4.88	0.975	1004
$H_{\mathrm{cell}} = 5$ mm	C2	0.075	4.82	0.963	1000
$P_{\mathrm{cell}} = 10$ mm	C3	0.1	4.76	0.950	995
	C4	0.25	4.42	0.878	972

The results of the first parametric study (Figs. 7–10) refer to the behaviour of a hygroscopic rotor with equal adsorption and desorption zones ($\tau_{\mathrm{ads}} = \tau_{\mathrm{des}}$), at a pressure of 101,325 Pa and for the particular inlet conditions indicated in Table 3. The channel wall is assumed to be composed by a desiccant layer without substrate and the length channel is fixed at $L_{\mathrm{c}} = 0.3$ m. For the case of the matrix cell B3 and $\tau_{\mathrm{cyc}} = 500$ s, Fig. 7 illustrates the time evolutions of the states of the interface and of the bulk flow in four sections at different longitudinal locations of the channel, as a function of the angular position, evidencing the abrupt variations after the mode transition. From the temperature and the moisture content evolutions (Fig. 7a and b), it can be observed that the airflow and the wall are closely in thermodynamic equilibrium in most of the rotor domain, a condition that is sometimes taken as a simplifying hypothesis in the behaviour analysis of ideal desiccant wheels (v., e.g. [46]). It can also be seen that only in the desorption mode the channel wall surface achieves equilibrium with the incoming air, an indication that the regeneration process is completed. This suggests that it is possible to optimise the dehumidification performance of the rotor

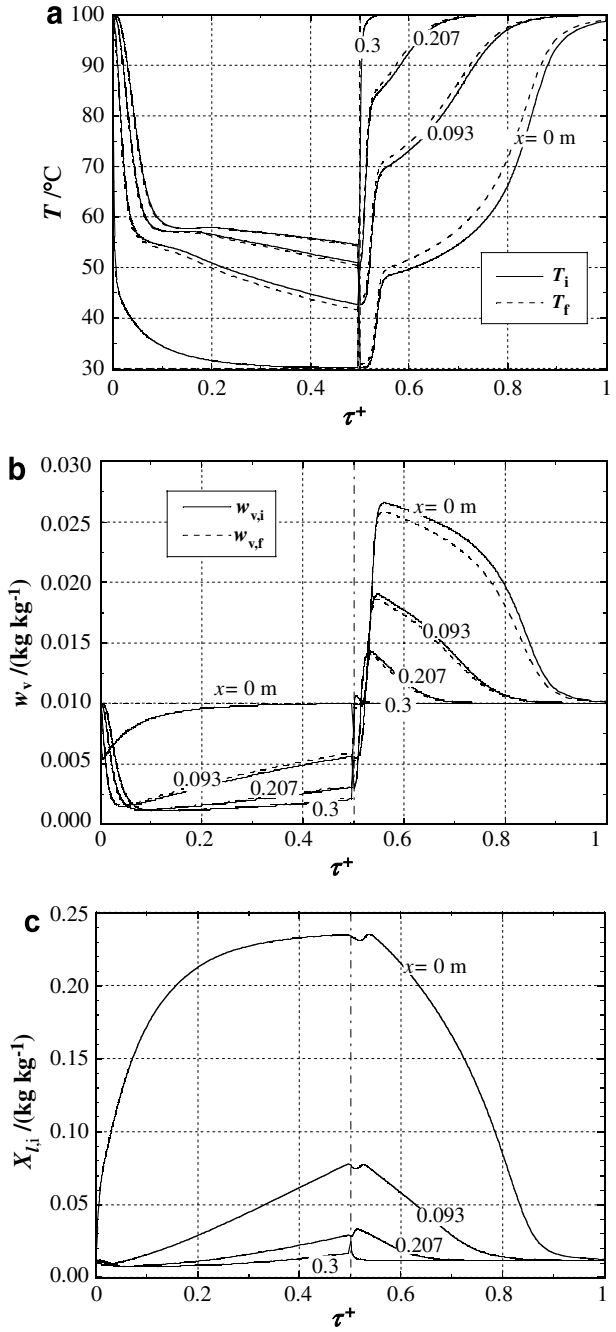

Fig. 7. Interface and airflow states (subscripts 's' and 'f') in four sections of the channel ($x = 0$; 0.093; 0.207 and 0.3 m), as a function of the angular position in the cycle: (a)temperature, (b) water vapour content and (c) adsorbed water content at interface. (Cell B3; $\tau_{cyc} = 500$ s, $\tau^+ = \tau/\tau_{cyc}$).

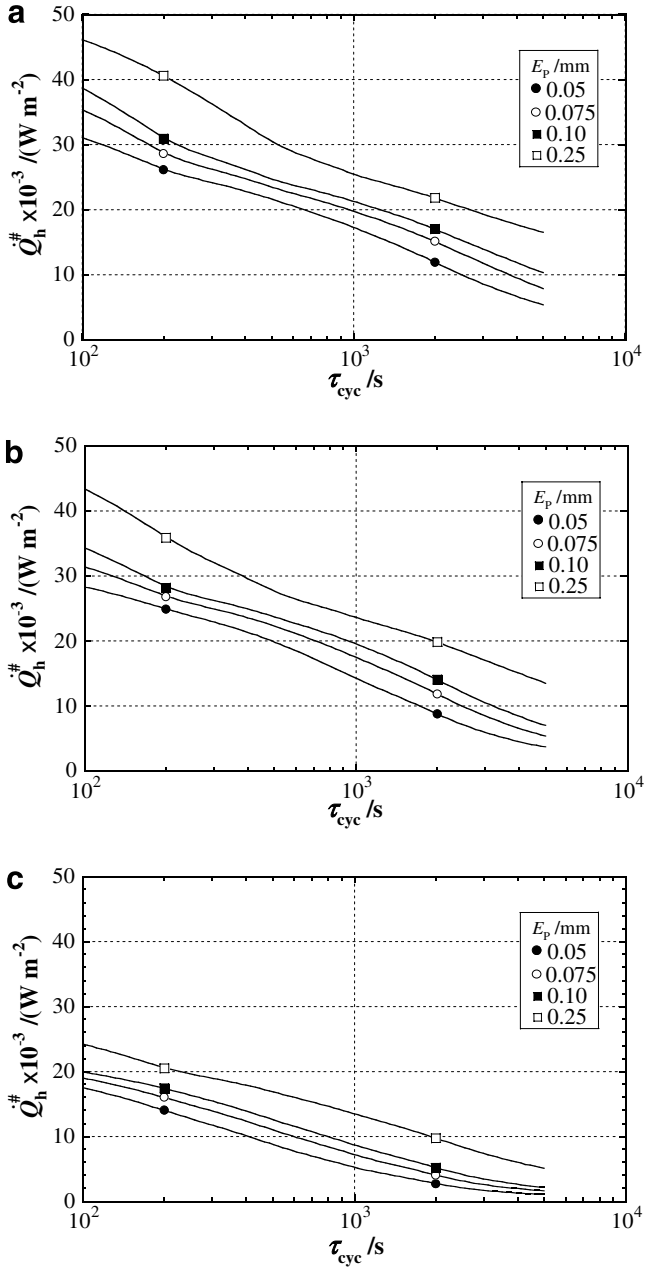

Fig. 8. Heat transfer rate per unit of frontal area of the hygroscopic rotor: (a) cells A, (b) cells B and (c) cells C.

through the reduction of the rotation speed and the augmentation of the adsorption zone.

The results of the parametric study are summarized in terms of the influences of τ_{cyc} and E_p on the global heat and mass transfer rates, for the three types of cells (Table 2). Figs. 8 and 9 represent, respectively, the heat and mass transfer rates per unit of frontal area of the matrix, while Fig. 10 shows the mass transfer rate per unit of transfer area. The heat transfer rates exhibit a monotonic decreasing trend with the cycle duration, with similar values in cells A and B, but rather lower values in cell C. Furthermore, it is observed that thicker channel walls provide higher heat transfer rates.

From Fig. 9, it is possible to identify for each cell type the optimal cycle duration that maximizes the dehumidification capacity of the desiccant wheel, and conclude that such optimum value depends strongly on the wall thickness of the channels. The maximum values of the mass transfer rate $\dot{J}_m^{\#}$ are close to 0.006 kg s^{-1} m^{-2}, for cells A and B, and about 0.005 kg s^{-1} m^{-2} for the cells of type C, regardless of the wall thickness.

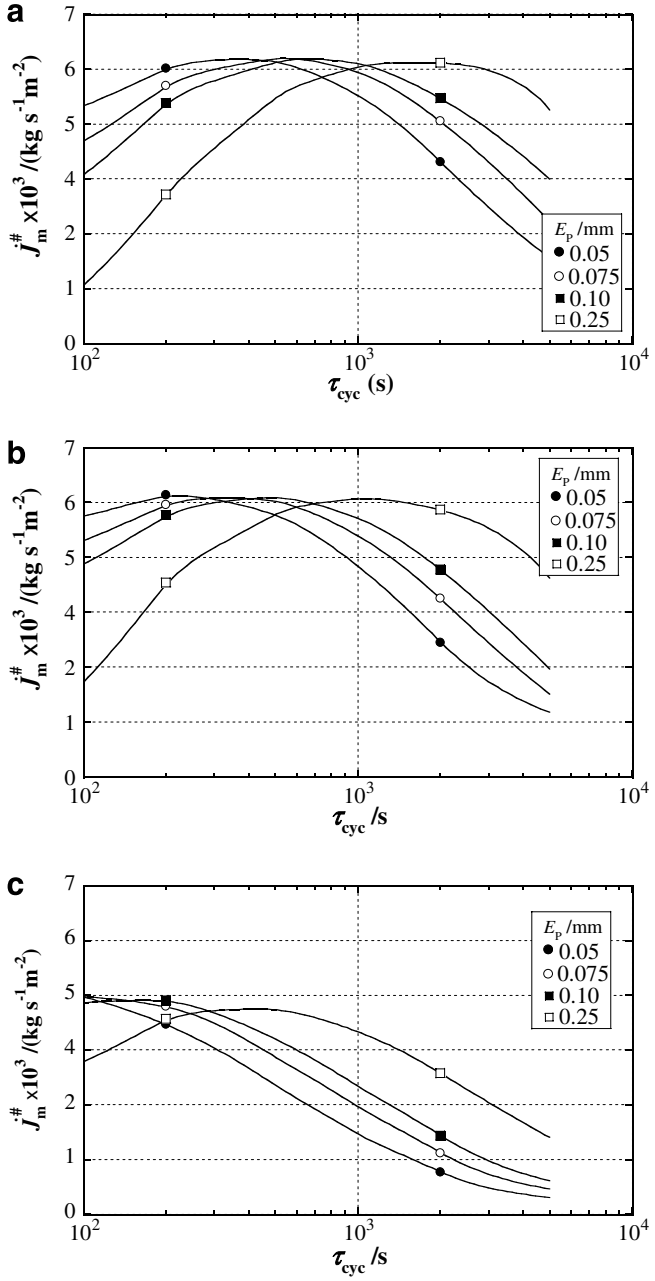

Fig. 9. Mass transfer rate per unit of frontal area of the hygroscopic rotor: (a) cells A, (b) cells B and (c) cells C.

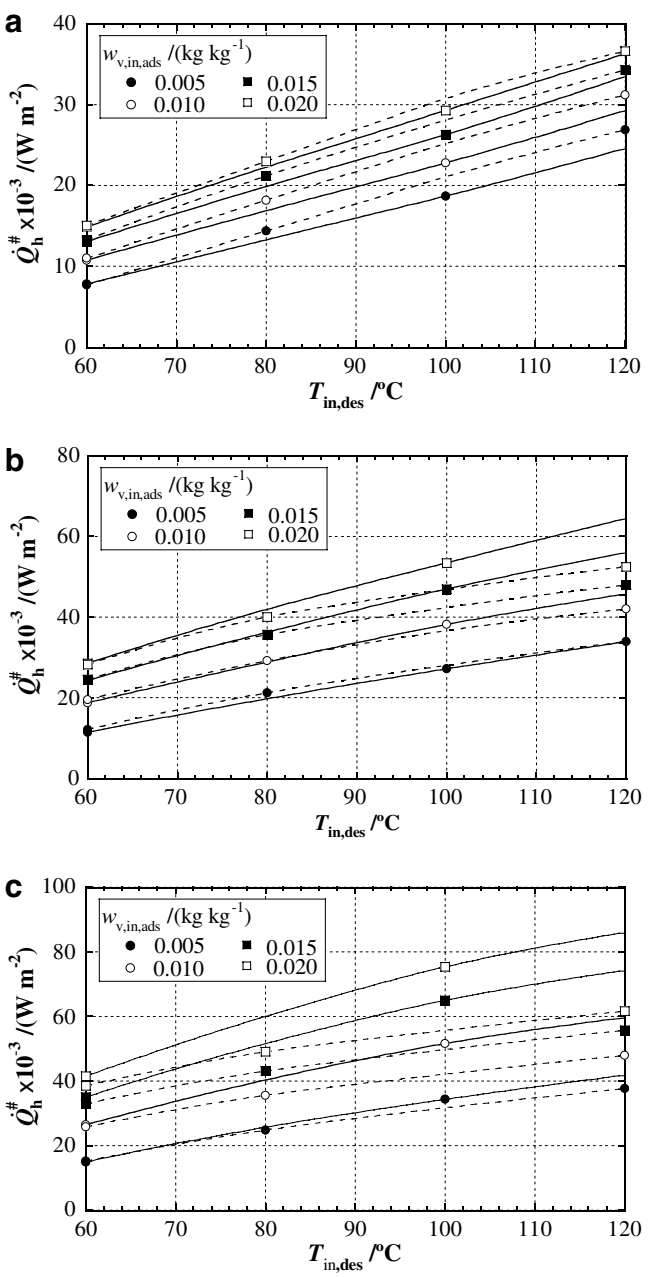

Fig. 10. Heat transfer rate per unit of frontal area of the hygroscopic rotor with cell B4 considering $F_{m,ads} = F_{m,des}$ and equal to: (a) 1 kg s^{-1} m^{-2}, (b) 2 kg s^{-1} m^{-2} and (c) 3 kg s^{-1} m^{-2}; (—: $H_d = 0.125$ mm, $H_{sub} = 0$; - - -: $H_d = 0.0125$ mm, $H_{sub} = 0.1$ mm).

In a next parametric study, two wall constitutions were analysed: one wall without substrate, and the other, a wall of type I with $H_{sub} = 0.1$ mm and $H_d = 0.025$ mm. In both cases, the length $L_c = 0.3$ m is maintained, and the thickness of the channel wall is fixed at $E_p = 0.25$ mm, ($H_p = 0.125$ mm), corresponding to the cell B4. The study is focussed on the influence of the inlet airflow conditions, as considered in Table 4, maintaining the pressure of 101,325 Pa and a fixed value of $\tau_{cyc} = 500$ s, for a wheel with equal adsorption and desorption zones ($\tau_{ads} = \tau_{des} = 250$ s).

For both wall constitutions considered, Figs. 10a–c show how the heat transfer rate $\dot{Q}^{\#}_h$ depends on the inlet temperature in the desorption zone and on the inlet water vapour content in the adsorption zone, for increasing airflow rates. The same influences on the mass transfer rate

Table 3
Inlet conditions of the airflows

	Adsorption zone	Desorption zone
T_{in} (°C)	30	100
$w_{v,in}$ (kg kg^{-1})	0.01	0.01
$F_{m,in}$ (kg s^{-1} m^{-2})	1.5	1.5

Table 4
Inlet conditions of the air flows

	Adsorption zone	Desorption zone
T_{in} (°C)	30	60, 80, 100, 120
$w_{v,in}$ (kg kg^{-1})	0.005, 0.01, 0.015, 0.02	0.01
$F_{m,in}$ (kg s^{-1} m^{-2})	1.0, 2.0, 3.0	1.0, 2.0, 3.0

$\dot{J}_m^{\#}$ are represented in Figs. 11a–c. It can be concluded that, as expected, the heat and mass transfer rates increase monotonically with the inlet temperature of the regeneration airflow, as well as with the inlet vapour content in the adsorption zone. Furthermore, it is seen from Fig. 11 that the dehumidification capacity is generally greater for the wall without substrate when the vapour content in the adsorption incoming air is higher ($w_{v,in,ads} > 0.010$ kg kg^{-1}), differences that are more notorious for higher airflow rates.

The influence of the same parameters on the outlet states of both airflows in the case of the channel wall without substrate is represented in Figs. 12 and 13. The results in

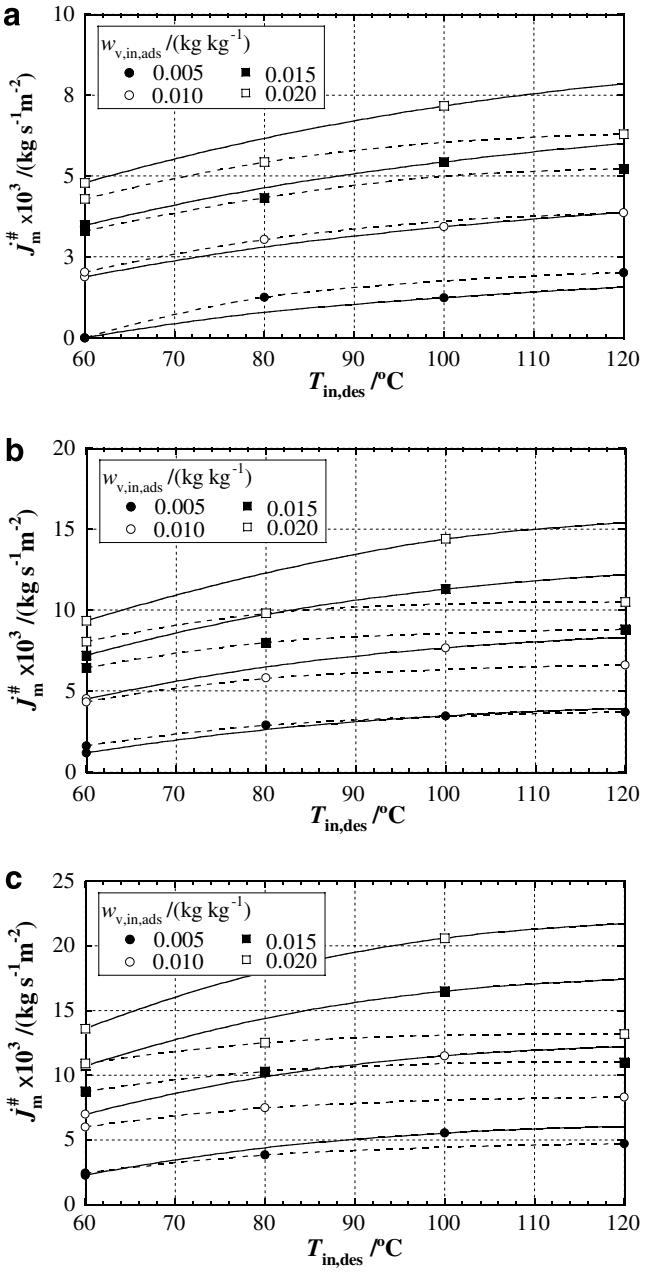

Fig. 11. Mass transfer rate per unit of frontal area of the hygroscopic rotor with cell B4, considering $F_{m,ads} = F_{m,des}$ and equal to: (a) 1 kg s^{-1} m^{-2}, (b) 2 kg s^{-1} m^{-2} and (c) 3 kg s^{-1} m^{-2}; (—: $H_d = 0.125$ mm, $H_{sub} = 0$; - - -: $H_d = 0.0125$ mm, $H_{sub} = 0.1$ mm).

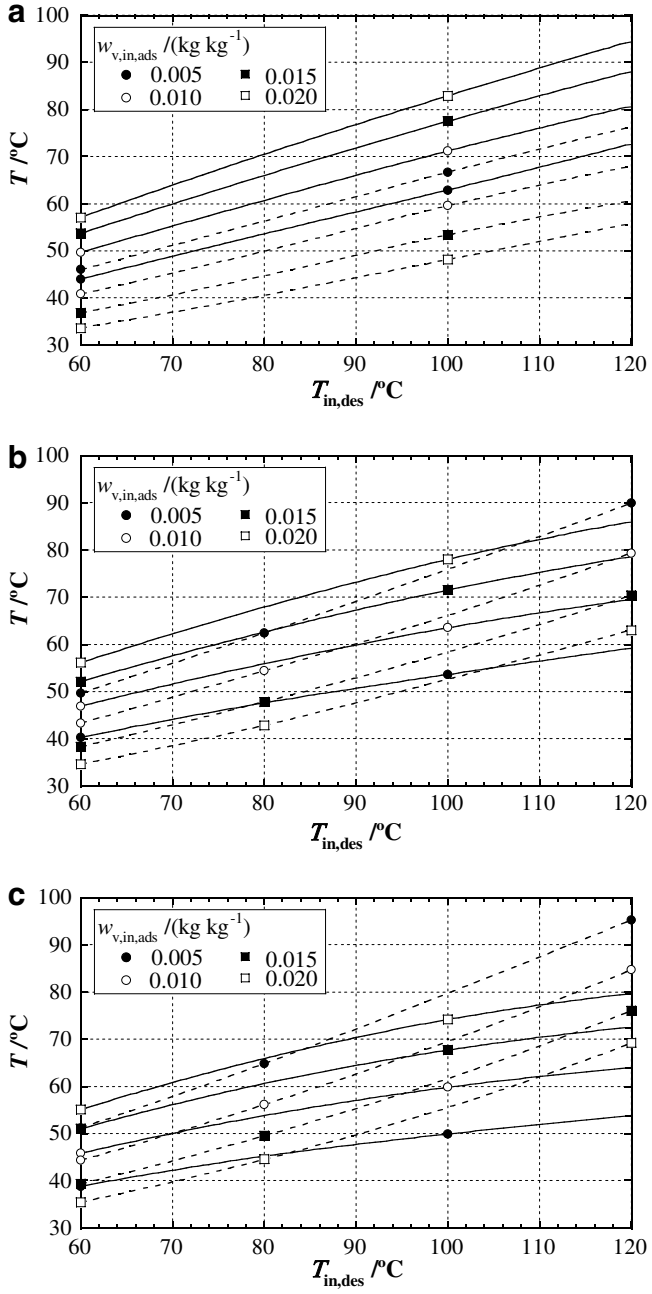

Fig. 12. Outlet temperatures in the adsorption and desorption zones of the hygroscopic rotor with cell B4, considering $F_{m,ads} = F_{m,des}$ and equal to: (a) 1 kg s^{-1} m^{-2}, (b) 2 kg s^{-1} m^{-2} and (c) 3 kg s^{-1} m^{-2}; (—: $T_{out,ads}$; – – – : $T_{out,des}$).

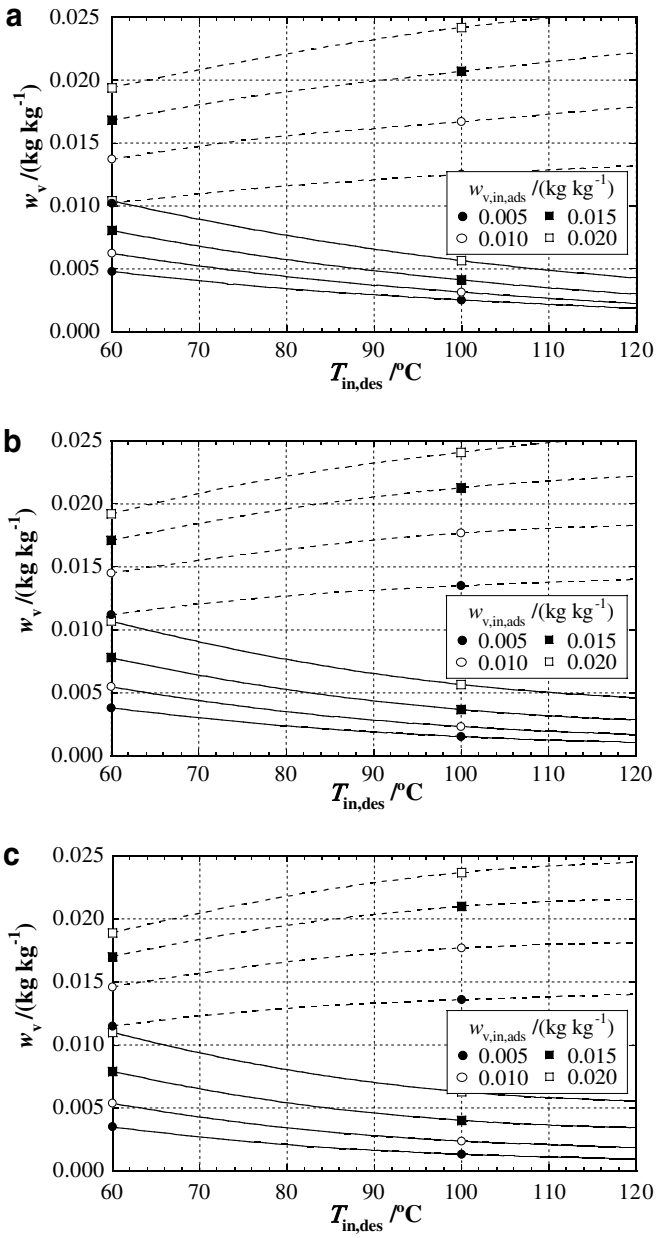

Fig. 13. Outlet water vapour content in the adsorption and desorption zones of the hygroscopic rotor with cell B4, considering $F_{m,ads} = F_{m,des}$ and equal to: (a) 1 kg s^{-1} m^{-2}, (b) 2 kg s^{-1} m^{-2} and (c) 3 kg s^{-1} m^{-2}; (—: $w_{v,out,ads}$; – – –: $w_{,out,des}$).

Fig. 13, particularly, allow to conclude that, even for relatively low values of the regeneration air temperature (say, $T_{in,des} \approx 80$ °C) and high values of $w_{v,in,ads}$, a good dehumidification effect can be achieved. This conclusion is particularly relevant for practical purposes, since it illustrates the possibility of using desiccant wheels in solar-powered desiccant evaporative cooling systems.

5. Conclusions

The simplified model MS presented in Part I was adapted to simulate the transient cyclic behaviour of hygroscopic rotors with real shape channels under uniform inlet flow conditions. The real channel is supposed to belong to a sinusoidal-type corrugated matrix and it is approached by an equivalent parallel plate configuration with the same wall thickness and the real ratio of airflow rate to wetted perimeter. The interaction between the bulk airflow and the interface is treated through convective transfer coefficients estimated from values of *Nu* and *Sh* numbers for laminar developed flow in real configurations.

Two parametric studies were performed for an equally partitioned desiccant wheel with a fixed, moderate channel length. The first one was focussed mainly on the influence of the cycle duration on the wheel performance, considering different cell dimensions and channel wall thicknesses, and it led to the conclusion that the maximum mass transfer rate per unit of frontal area is practically independent of the channel wall thickness. However, higher rotation speeds should be adopted for thinner channel walls. The second study was conducted to analyse the influence of the regeneration air temperature and of the vapour content in the incoming air for the adsorption zone, considering two wall constitutions and different airflow rates. The results illustrate the potentialities of the model in mapping the global heat and mass transfer performance of hygroscopic rotors, which is a relevant information for design purposes, namely in industrial dehumidification applications and for desiccant evaporative cooling systems.

A lack of information for the complete characterization of the desiccant media, as required for the validation of detailed numerical models, deserves an additional exhaustive experimental research to determine the properties of different desiccant media. Moreover, some preliminary work must be done coupling specific experiments and numerical simulation to derive the needed correlations, particularly for the surface diffusion coefficient.

References

[1] W. Jin, A. Kodama, M. Goto, T. Hirose, An adsorptive desiccant cooling using honeycomb rotor dehumidifier, J. Chem. Eng. Japan 31 (5) (1998) 706–713.

[2] E.A. Vineyard, J.R. Sand, D.J. Durfee, Parametric analysis of variables that affect the performance of a desiccant dehumidification system, ASHRAE Trans. 106 (1) (2000).

[3] E.A. Vineyard, J.R. Sand, D.J. Durfee, Performance characteristics for a desiccant system at two extreme ambient conditions, ASHRAE Trans. (2002) 587–596.

[4] M. Kanoğlu, M.Ö. Çarpınlıoğlu, M. Yıldırım, Energy and exergy analyses of an experimental open-cycle desiccant cooling system, Appl. Therm. Eng. 24 (5–6) (2004) 919–932.

[5] M.Ö. Çarpınlıoğlu, M. Yıldırım, M. Kanoğlu, Experimental study on an open cycle desiccant cooling system, Int. J. Exergy 1 (2) (2004) 268–288.

[6] A. Kodama, W. Jin, M. Goto, T. Hirose, M. Pons, Entropic analysis of adsorption open cycles for air conditioning Part 2: interpretation of experimental data, Int. J. Energy Res. 24 (3) (2000) 263–278.

[7] M. Pons, A. Kodama, Entropic analysis of adsorption open cycles for air conditioning Part 1: first and second law analysis, Int. J. Energy Res. 24 (3) (2000) 251–262.

[8] J.R. Camargo, C.D. Ebinuma, J.L. Silveira, Thermoeconomic analysis of an evaporative desiccant air conditioning system Part 2: interpretation of experimental data, Appl. Therm. Eng. 23 (12) (2003) 1537–1549.
[9] S.P. Halliday, C.B. Beggs, P.A. Sleigh, The use of solar desiccant cooling in the UK: a feasibility study, Appl. Therm. Eng. 22 (12) (2002) 1327–1338.
[10] W.A. Belding, M.P.F. Delmas, W.D. Holeman, Desiccant aging and its effects on desiccant cooling system performance, Appl. Therm. Eng. 16 (5) (1996) 447–459.
[11] M. Czachorski, J. Wurm, W.M. Worek, J. Mierke, P. Brillhart, Dynamic testing of desiccant matrices and computerized evaluation of performance maps, ASHRAE Trans. 103 (Part 1) (1997) 833–840.
[12] L. Bellia, P. Mazzei, F. Minichiello, D. Palma, Air conditioning systems with desiccant wheel for Italian climates, Int. J. Archit. Sci. 01 (4) (2000) 193–213.
[13] P. Mazzei, F. Minichiello, D. Palma, Desiccant HVAC systems for commercial buildings, Appl. Therm. Eng. 22 (5) (2002) 545–560.
[14] C.B. Beggs, S. Halliday, A theoretical evaluation of solar-powered desiccant cooling in the United, Build. Serv. Eng. Res. Technol. 20 (3) (1999) 113–117.
[15] A.A. Pesaran, A. Mills, Moisture transport in silica gel packed beds-II experimental study, Int. J. Heat Mass Transfer 30 (6) (1987) 1051–1060.
[16] K. Schultz, Rotary solid desiccant dehumidifiers – analysis of models and experimental investigation, Ph.D thesis, University of Wisconsin, Madison, 1987.
[17] Y.K. Chuah, P. Norton, F. Kreith, Transient mass transfer in parallel passage dehumidifiers with and without solid side resistance, ASME J. Heat Transfer 111 (4) (1989) 1038–1044.
[18] T. Kravchik, E. Korin, I. Borde, Influence of material properties and heat removal on mass and heat transfer in a solid desiccant dehumidifier, Chem. Eng. Proc. 27 (1) (1990) 19–25.
[19] E. Van den Bulck, Transient heat and mass transfer in laminar flow forced convection in ducts, Int. J. Heat Mass Transfer 34 (4/5) (1991) 1249–1258.
[20] S. Neti, E.I. Wolfe, Measurements of effectiveness in a silica gel rotary exchanger, Appl. Therm. Eng. 20 (4) (2000) 309–322.
[21] J.M. Cejudo, R. Moreno, A. Carrillo, Physical and neural network models of a silica gel desiccant wheel, Energy Buildings 34 (8) (2002) 837–844.
[22] M.H. Ahmed, N.M. Kattab, M. Fouad, Evaluation and optimization of solar desiccant wheel performance, Renew. Energy 30 (3) (2005) 305–325.
[23] A. Kodama, T. Hirayama, M. Goto, T. Hirose, R.E. Critoph, The use of psychrometric charts for the optimisation of a thermal swing desiccant wheel, Appl. Therm. Eng. 21 (16) (2001) 1657–1674.
[24] M. Beccali, F. Butera, R. Guanella, R.S. Adhikari, Simplified models for the performance evaluation of desiccant wheel dehumidification, Int. J. Energy Res. 27 (1) (2003) 17–29.
[25] M. Beccali, R.S. Adhikari, F. Butera, V. Franzitta, Short communication-update on desiccant wheel model, Int. J. Energy Res. 28 (12) (2004) 1043–1049.
[26] S. Murali Krishna, S. Srinivasa Murthy, Experiments on silica gel rotary dehumidifier, Heat Recov. Syst. CHP 9 (5) (1989) 467–473.
[27] A. Kodama, M. Goto, T. Hirose, T. Kuma, Experimental study of optimal operation for a honeycomb adsorber operated with thermal swing, J. Chem. Eng. Japan 26 (5) (1993) 530–535.
[28] A. Kodama, M. Goto, T. Hirose, T. Kuma, Temperature profile and optimal rotation speed of a honeycomb rotor adsorber operated with thermal swing, J. Chem. Eng. Japan 27 (5) (1994) 644–649.
[29] A. Kodama, T. Kuma, Performance evaluation for a thermal swing honeycomb rotor adsorber using a humidity chart, J. Chem. Eng. Japan 28 (1) (1995) 19–24.
[30] C.J. Simonson, R.W. Besant, Heat and moisture transfer in desiccant coated rotary energy exchangers: Part II validation and sensitivity studies, Int. J. HVAC&R Res. 3 (4) (1997) 351–368.
[31] C.J. Simonson, D.L. Ciepliski, R.W. Besant, Determining the performance of energy wheels: Part I-experimental and numerical methods, ASHRAE Trans. 105 (1) (1999).
[32] C.J. Simonson, D.L. Ciepliski, R.W. Besant, Determining the performance of energy wheels: Part II-experimental data and numerical validation, ASHRAE Trans. 105 (1) (1999).
[33] W. Shang, R.W. Besant, Energy wheel effectiveness evaluation: Part I-outlet airflow property distributions adjacent to an energy wheel, ASHRAE Trans. 107 (2) (2001).
[34] W. Shang, R.W. Besant, Energy wheel effectiveness evaluation: Part II-testing and monitoring energy wheels in HVAC applications, ASHRAE Trans. 107 (2) (2001).
[35] D. Charoensupaya, W.M. Worek, Effects of adsorbent heat and mass transfer resistances on the performance of an open-cycle adiabatic desiccant cooling system, Heat Recov. Syst. CHP 8 (6) (1988) 537–548.
[36] P. Majumdar, Heat and mass transfer in composite pore structures for dehumidification, Sol. Energy 62 (1) (1998) 1–10.
[37] L.A. Sphaier, W.M. Worek, Analysis of heat and mass transfer in porous sorbents used in rotary regenerators, Int. J. Heat Mass Transfer 47 (14–16) (2004) 3415–3430.
[38] J.L. Niu, L.Z. Zhang, Effects of wall thickness on the heat and moisture transfer in desiccant wheels for air dehumidification and enthalpy recovery, Int. Comm. Heat Mass Transfer 29 (2) (2002) 255–268.
[39] L.Z. Zhang, J.L. Niu, Performance comparisons of desiccant wheels for air dehumidification and enthalpy recovery, Appl. Therm. Eng. 22 (12) (2002) 1347–1367.
[40] L.Z. Zhang, J.L. Niu, A pre-cooling Munters environmental control desiccant cooling cycle in combination with chilled-ceiling panels, Energy 28 (3) (2003) 275–292.
[41] C.R. Ruivo, Modelação numérica dos fenómenos de transferência de calor e de massa em rodas higroscópicas, Ph.D. thesis, University of Coimbra, Coimbra, Portugal, 2005.
[42] X.J. Zhang, Y.J. Dai, R.Z. Wang, A simulation study of heat and mass transfer in a honeycomb rotary desiccant dehumidifier, Appl. Therm. Eng. 23 (8) (2003) 989–1003.
[43] Y. Çengel, Heat transfer – a practical approach, McGraw-Hill, 1998.
[44] F.P. Incropera, D.P. DeWitt, Fundamentals of heat and mass transfer, 5th ed., John Wiley, 1996.
[45] J.L. Niu, L.Z. Zhang, Heat transfer and friction coefficients in corrugated ducts confined by sinusoidal and arc curves, Int. J. Heat Mass Transfer 45 (3) (2003) 571–578.
[46] E. Van Den Bulk, J.W. Mitchell, S.A. Klein, Design theory for rotary heat and mass exchangers-I, wave analysis of rotary heat and mass exchangers with infinite transfer coefficients, Int. J. Heat Mass Transfer 28 (8) (1985) 1575–1586.